Physical Chemistry Chemical Physics

PCCP

Controlling the growth mode of para-sexiphenyl (6P) on ZnO by partial fluorination

Journal:	*Physical Chemistry Chemical Physics*
Manuscript ID:	CP-ART-09-2014-004048.R1
Article Type:	Paper
Date Submitted by the Author:	20-Oct-2014

Complete List of Authors:	Sparenberg, Mino; Humboldt Universität zu Berlin, Institut für Physik Zykov, Anton; Humboldt Universität zu Berlin, Institut für Physik Beyer, Paul; Humboldt Universität zu Berlin, Institut für Physik Pithan, Linus; Humboldt Universität zu Berlin, Institut für Physik Weber, Christopher; Humboldt Universität zu Berlin, Institut für Physik Garmshausen, Yves; Humboldt Universität zu Berlin, Institut für Chemie Carlà, Francesco; ESRF, Experiment Division Hecht, Stefan; Humboldt Universität zu Berlin, Institut für Chemie BLUMSTENGEL, Sylke; Humboldt Universität zu Berlin, Institut für Physik Henneberger, Fritz; Humboldt Universität zu Berlin, Institut für Physik Kowarik, Stefan; Humboldt Universität zu Berlin, Institut für Physik

Title: Controlling the growth mode of *para*-sexiphenyl (6P) on ZnO by partial fluorination

M. Sparenberg*, A. Zykov*, P. Beyer, L. Pithan, C. Weber, Y. Garmshausen, F. Carlà, S. Hecht, S. Blumstengel, F. Henneberger, S. Kowarik

*these authors contributed equally, A. Z. performed X-ray analysis and M. S. performed AFM analysis

Abstract:

We report on the impact of partial fluorination of *para*-sexiphenyl (6P) on the growth mode when deposited on the non-polar ZnO$(10\bar{1}0)$ surface. The evolution of the thin film structure and morphology is monitored by *in situ* atomic force microscopy and *in situ* real-time X-ray scattering. Both 6P and its symmetrical, terminally fluorinated derivative (6P-F_4) grow in a highly crystalline mode, however, with a distinctly different morphology. While 6P films are characterised by the formation of two different phases with three-dimensional nanocrystallites and consequently a rather rough surface morphology, layer-by-layer growth and phase purity in case of 6P-F_4 prevails leading to smooth terraced thin films. We relate the different growth behaviour to specifics of the thin film structure.

1 Introduction

Hybrid structures of inorganic and organic semiconductors (HIOS) have attracted significant attention in recent years as the combination makes it possible to realize material properties that cannot be achieved with either material alone. Inorganic semiconductors, for example, have superior charge carrier mobilities compared to organic materials, while conjugated molecules offer strong optical absorption and emission. In combination with the efficient charge- as well as efficient exciton-transfer across the inorganic/organic interface that has been demonstrated for example in ZnO/organic HIOS[1] these material combinations are highly attractive for opto-electronic applications such as light-emitting devices or photovoltaic cells.

For the functionality of HIOS, the interface structure and morphology of the molecular component are of great importance. Highly crystalline molecular morphologies with low surface roughness are frequently demanded, *e.g.* when targeting a higher charge carrier mobility.[2] The molecular structure close to the interface often differs from the bulk phase and is modified by the interaction with the substrate,[3–5] sometimes with adverse consequences for the electronic and optical properties. In many cases, crystalline films do not build up in a smooth layer-by-layer regime. Instead roughening and island growth prevails. Growth temperature and molecular deposition rate provide some control, but are mostly not sufficient to achieve the desired structural perfection. Another interesting alternative to obtain control over the growth process is chemical modification of the organic molecule.[6,7] The challenge is to maintain the optical properties of the molecules, while purposefully altering the molecule-molecule and molecule-substrate interaction in order to chemically tune the HIOS growth mode.

Here we compare the prototypical organic semiconductor *para*-sexiphenyl (6P, $C_{36}H_{26}$) with its symmetrical, terminally fluorinated derivative 6P-F_4 ($C_{36}H_{22}F_4$) (Fig. 1a and b) focussing on HIOS where the molecules are assembled on the non-polar $(10\bar{1}0)$ surface of ZnO (see Fig. 1c and d). The molecules possess indeed identical optical absorption and fluorescence spectra (supporting information (SI) part A). 6P is a promising candidate as light-emitter in opto-electronic applications[8–11] and its structure and growth mode has been already studied on various substrates.[2,12–16] Mostly a so called β-structure[17] (a = 8.091 Å, b = 5.568 Å, c = 26.241 Å, α = 90°, β = 98.17°, γ = 90°) is observed, however, in thin films grown at elevated substrate temperature, also the γ-structure has been found (a = 7.98 Å, b = 5.54 Å, c = 27.64 Å, α = 90°, β = 99.8°, γ = 90°).[18] In a previous study we found that alternating rows of Zn and O ions create an electrostatic surface field that acts as a template for ordering of 6P molecules.[15,19] Growth of 6P-F_4 has not been studied yet and its crystal structure is so far unknown.

In what follows we demonstrate that fluorination indeed alters the growth mode from three-dimensional (3D) in case of 6P, leading to films composed of nanocrystallites with preferential in- and out-of-plane orientation,[15,19] to comparatively smooth, two-dimensional (2D) layer-by-layer growth for 6P-F_4. The terminally fluorinated molecule grows in a single phase, whereas two different phases coexist in 6P films on ZnO. Furthermore, we find that 6P-F_4 growth proceeds via a wetting layer and a surface induced structure exists in which the molecular tilt angle changes from more upright to a more inclined orientation.

To uncover differences in the growth modes for 6P and its fluorinated species and to elucidate the structural properties of sub- and multilayers, we performed a combined X-ray scattering and atomic force microscopy (AFM) analysis. First, a comparative post growth overview between layers of 6P and 6P-F_4 is given based on the AFM surface morphology and X-ray measurements. Second, the development of the molecular morphology from sub- to a few monolayer (ML) coverage is studied by AFM, where we restrict ourselves to the presentation of AFM data for 6P-F_4, as 6P has been extensively investigated in previous studies.[2,15,20–22] Finally the film growth dynamics of both, 6P and 6P-F_4, are examined by real-time X-ray reflectivity (XRR) experiments and compared to the AFM morphology at corresponding growth steps.

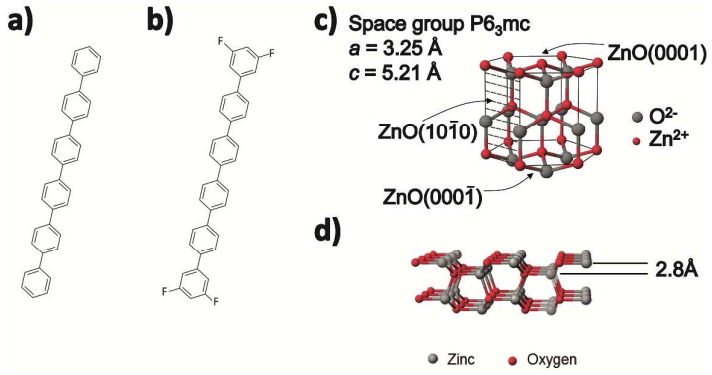

Fig. 1: a) and b) schematic molecular structures of 6P and 6P-F_4. c) Sketch of the ZnO crystal structure. d) Side view of the (10$\bar{1}$0) ZnO surface.

2 Experimental

2.1 Substrate treatment and organic film deposition:

Organic films were grown by organic molecular beam deposition (OMBD) on ZnO($10\bar{1}0$) wafers (CrysTec GmbH, Germany) in ultrahigh vacuum (UHV) systems allowing for *in situ* AFM on the one hand and *in situ* real-time X-ray studies on the other hand. The substrate was kept at room temperature during molecule deposition and all measurements.

For the X-ray experiments, an atomically flat, terraced surface is obtained adopting the procedure proposed by Götzen *et al*..[23] In a first step, the substrates were sputtered for 1 h in vacuum with Ar^+-ions (1 keV). In a second step, the substrates were annealed for 3 h in ambient air at a temperature of 950 °C. Afterwards, the organic films were grown by OMDB in a mobile UHV chamber at a base pressure of <1.0 x 10^{-9} mbar. The deposition rate was kept constant at 0.6 Å/min in the case of 6P-F_4 and at 1.3 Å/min in the case of 6P.

For the *in situ* UHV-AFM investigations, the ZnO($10\bar{1}0$) films were grown in a dual chamber system (DCA). Before deposition of the molecules, ZnO wafers were overgrown with a 100 nm thick ZnO epilayer by radical source molecular beam epitaxy at a base pressure of 1.0 x 10^{-10} mbar to assure a well-defined pristine surface.[24] Subsequently, the samples were transferred to the interconnected "organic" growth chamber at a base pressure of 1.0 x 10^{-9} mbar. The deposition rates for 6P-F_4 and 6P were kept constant at ≈1…1.5 Å/min as monitored by a quartz microbalance positioned next to the sample.

2.2 Molecules:

Para-sexiphenyl ($C_{36}H_{26}$, 6P) was obtained from TCI Deutschland GmbH. The fluorinated 6P-F_4 ($C_{36}H_{22}F_4$) was synthesized via a Ni-catalysed homocoupling of the corresponding 4-bromoterphenyl.[25] The product is as insoluble as the parent 6P and was therefore purified by extensive washing and repeated recrystallization [for details, see SI part B].

2.3 *In situ* atomic force microscopy (AFM) measurements:

AFM measurements were performed with an UHV-AFM/STM (Omicron) at a base pressure of 1.0 x 10^{-9} mbar and controlled by a Matrix system. The analysis chamber is connected to the growth chambers via a buffer system to allow for *in situ* measurements. The AFM was operated in non-contact mode using PtIr-coated cantilevers (PPP-EFM, Nanosensors) with a resonance frequency of 75 kHz. The *z*-height calibration of the AFM was checked by measuring the step height of adjacent ZnO terraces on the Ar^+-ion sputtered substrate. The AFM images were processed using the open source software Gwyddion.[26]

2.4 *In situ* and real-time X-ray scattering measurements:

All X-ray scattering experiments were performed at the ID03 beamline of the European Synchrotron Radiation Facility (ESRF Grenoble, France) at a wavelength of λ = 1.305 Å. The experimental data was acquired using a MAXIPIX photon-counting detector. During the thin-film growth the intensity of the specular reflected X-ray beam (XRR) was monitored in real-time in a reciprocal wave vector range from q_z = 0.025 Å^{-1} up to q_z = 0.34 Å^{-1} to investigate the evolution of the out-of-plane structure. The time resolution of below 2 min per scan enables sub-monolayer resolution as it is fast compared to the deposition time of ~26 min per ML at the chosen growth rate of ~1 Å/min. Complementary post-growth Θ-2Θ-X-ray diffraction (XRD) and grazing incidence X-ray diffraction (GIXD) measurements were performed to study the out-of- and in-plane structures of several ML thick films. All presented XRR and XRD data contain a geometrical footprint correction and the diffuse scattering is subtracted to obtain the true specular reflectivity.

3 Results

3.1 Overview:

Complementary AFM and XRD measurements reveal characteristic features of the morphology and structure of thin 6P and 6P-F_4 films (Fig. 2). The AFM image of a 5 nm thick 6P film on ZnO($\mathbf{10\bar{1}0}$) (Fig. 2a) demonstrates the formation of terraced, mound-like 3D islands with constant step heights of 2.6 nm ± 0.3 nm, as seen by the cross profile in Fig 2a. The 3D islands are thus composed of up to three MLs of nearly upright-standing molecules. The mounds have a regular polygonal form with a preferred in-plane orientation. The comparison with the equilibrium crystal shape (inset Fig. 2a)[27] implies that the 3D islands are composed of single crystallites with 6P[$\mathbf{010}$] parallel to ZnO[$\mathbf{001}$] and 6P($\mathbf{001}$) as the contact plane. On top of the mounds, needle-shaped crystallites orientated parallel to ZnO[$\mathbf{001}$] are visible as well. The needles are composed of flat lying molecules with 6P$\left(\mathbf{20\bar{3}}\right)$ forming the contact plane and the long molecular axis parallel to ZnO[$\mathbf{010}$].[15] For a single 6P molecule deposited on ZnO($\mathbf{10\bar{1}0}$), a preferential alignment parallel to the alternating rows of oxygen and zinc ions, *i.e.* parallel to ZnO[$\mathbf{010}$] was demonstrated as a consequence of the electrostatic interaction with the dipolar surface field.[19] Such aligned molecules are the precursors in the growth of both mounds and needles and thus explain the observed preferential orientation. Mound formation, though setting in at a later growth stage, was observed before in 6P films grown on ion-bombarded mica surfaces and assigned to a significant Ehrlich-Schwoebel barrier, hampering interlayer mass transport and leading to a rather rough surface morphology.[20] In contrast, fluorinated 6P-F_4 grows in extended 2D islands with irregular shape (Fig. 2b). Though the film is

nominally slightly thicker (6 nm), the third layer has barely started to nucleate yet. 6P-F_4 is thus characterized by a rather smooth surface morphology. The root mean square (RMS) roughness is only 0.8 nm as compared to 3.2 nm for 6P including needle-shaped crystallites and 1.7 nm excluding them from the analysis.

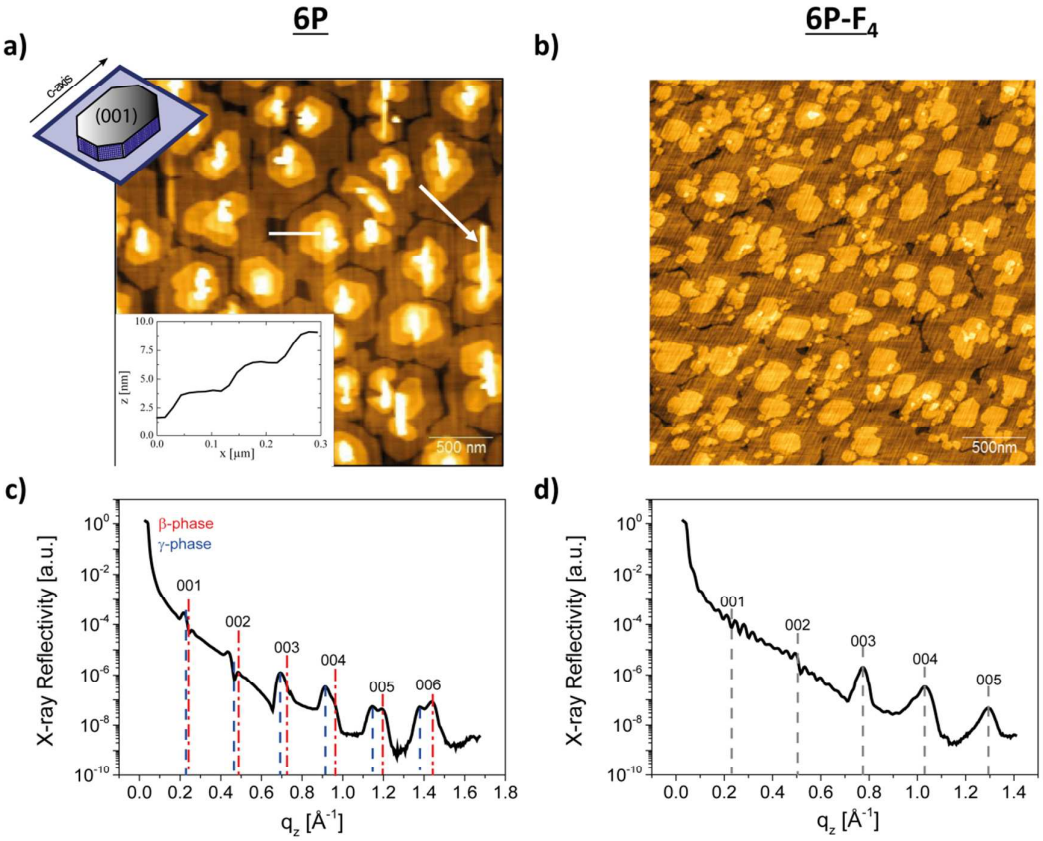

Fig. 2. AFM images (3 µm x 3 µm) with corresponding cross profile for 6P recorded along the white line of a nominally 5 nm thick 6P layer measured *ex situ* (a) and a nominally 6 nm thick 6P-F_4 layer measured *in situ* (b). Both films were grown at room temperature on ZnO$(10\bar{1}0)$. The inset shows the equilibrium crystal shape of 6P[27], which is observed to form on epitaxial ZnO with a preferential alignment. An arrow points towards the needles on top of the 6P mounds. X-ray reflectivity scans of ~18 nm thick 6P (c) and 6P-F_4 (d) films show Bragg reflections up to high order, which indicates high crystalline order. 6P films exhibit both β- and γ- phase Bragg reflections as indicated by the blue and red lines.

Further differences in the crystalline properties are revealed by XRD $\boldsymbol{\theta}$-2$\boldsymbol{\theta}$-scans (Figs. 2c, d) yielding the out-of-plane structure. The experiments are performed *in situ* on ~18-nm thick films. For both molecules ($\mathbf{00}\boldsymbol{l}$) Bragg reflections along the specular rod are visible at least up to the 5th order, which is evidence for nearly upright standing molecules and high structural order in both 6P and 6P-F_4 films. We note that the first and second order peaks are not well-pronounced, which is due to interferences between the comparatively strong ZnO substrate reflectivity and the molecular Bragg reflection, whose phase changes by π in the vicinity of the Bragg reflection. At higher q_z values, the

substrate reflectivity decreases rapidly, so the molecular Bragg reflections become more pronounced. For 6P the higher order peaks are clearly split corresponding to an average lattice spacing of $d_{6P,\beta}$ = 2.59 nm (corresponding to a tilt angle of 17°) and $d_{6P,\gamma}$ = 2.72 nm respectively, which are assigned to the known β- and *γ*-polymorphs of 6P.[17,18] Reflections of both polymorphs are of comparable strength, indicating that both phases nucleate and grow in parallel. This is in contrast with previous studies on glass, where pure β-phase and *γ*-phase growth was found for 6P at room and elevated substrate temperatures (160 °C), respectively.[18]

For 6P-F_4, an average lattice spacing of 2.42 ± 0.03 nm for a ~18 nm thick film is derived from the q_z values of the Bragg reflections. This demonstrates that the fluorinated 6P derivative grows in a different crystal structure than 6P resulting in a larger tilt of the molecules. Taking into account that the length between the terminal H-atoms in 6P-F4 is 2.72 nm just as in 6P, from the lattice constant we can estimate the molecular tilt angle to be 27° in the 3ML. Another difference is the occurrence of almost undamped Laue oscillations around the 1st and 2nd order Bragg reflections of 6P-F_4. These oscillations are evidence of a laterally homogeneous coherent thickness, *i.e.*, a well-defined number of ordered 6P-F_4 layers. 6P, on the other hand, does not show Laue oscillations indicating a rough surface.

3.2 Evolution of the of 6P-F_4 thin film morphology:

To uncover the evolution of the thin film morphology with exposure time, growth interruptions were introduced and *in situ* non-contact AFM snapshots taken (Fig 3a). Strikingly, after 2 min molecular exposure, no island formation of 6P-F_4 is yet observed. The amount of deposited molecules corresponds to roughly one ML of flat lying molecules assuming a sticking coefficient of one. The AFM image displays a corrugated surface with extended terraces parallel to ZnO$[0001]$, typical for epitaxial ZnO$(10\bar{1}0)$ surfaces. Formation of islands is only observed after an exposure time of 4 min. Continuing the deposition, the islands grow and eventually (after 30 min exposure) coalesce. The height of the islands in the sub-ML regime is 1.6 nm ± 0.3 nm (inset Fig. 3a), *i.e.*, is considerably smaller than the average lattice parameter deduced above from Θ-2Θ-XRD scans of thick 6P-F_4 films. The shape of the islands is slightly elongated along ZnO$[0001]$ with an aspect ratio of approximately 1.5 hinting at diffusion anisotropy. Nucleation of the second layer sets in at a coverage of the ZnO surface with islands of almost 90 %. Also the 3rd and 4th layer only start to grow when the underlying layer has almost completely formed as will be shown in more detail below by real-time X-ray data.

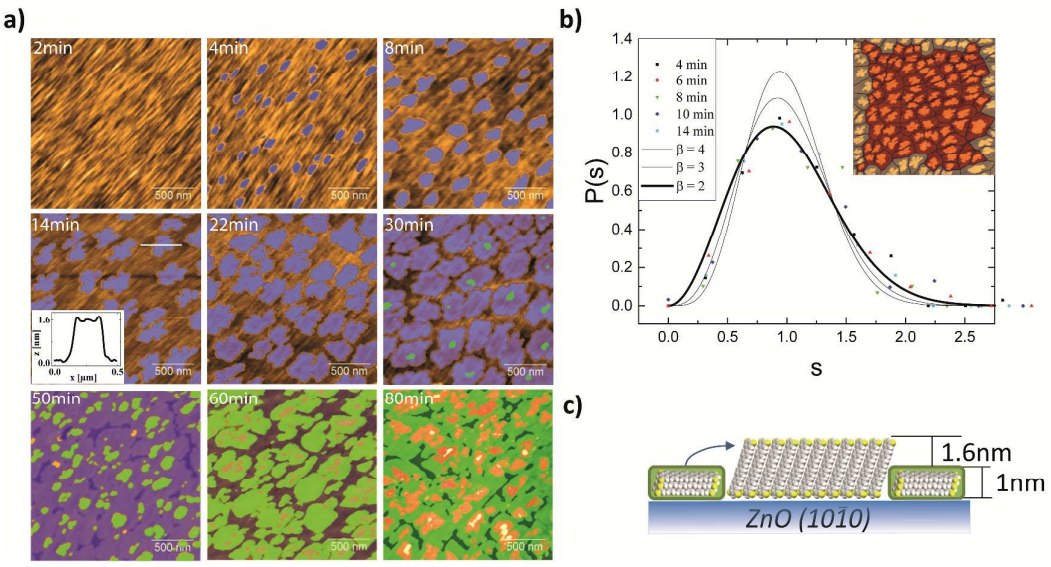

Fig. 3: Series of AFM images of 6P-F_4 deposited on the ZnO$(10\bar{1}0)$ surface for increasing exposure time. The 1st, 2nd, 3rd and 4th molecular layer are highlighted in blue, green, red and white respectively. The inset (14 min exposure) shows the height profile measured along the white line. (b) Voronoi tessellation of 4 µm x 4 µm AFM image recorded after 14 min exposure. Capture zone distributions (symbols) derived from AFM images recorded after exposure times between 4 and 22 min. The solid lines correspond to scaling functions with parameter $\beta = 2 - 4$. For details, see text. (c) Schematic depiction of the 6P-F_4 morphology in the initial stages of growth. Please note that the actual arrangement of the molecules in the wetting layer is not known.

In the following, we take a closer look at the sub-ML growth performing two different experiments. First, an additional AFM scan in contact mode is carried out after an exposure time of 10 min in the area between the islands. The applied force is chosen sufficiently high to push away a soft molecular layer by the tip. Recording subsequently a non-contact AFM image containing the scratched area reveals the formation of a trench of about 1.0 nm±0.3 nm depth (cross section profile in SI part D). Consequently, a wetting layer is present in the space between the islands that follows exactly the surface morphology of the ZnO surface. The arrangement of 6P-F_4 in this wetting layer is not known, however, the thickness implies that it is either composed of more than one layer of flat lying molecules as for instance in the case of Rubicene on SiO_2[28] or the molecules are tilted. It should be noted that we did not find evidence for the existence of a wetting layer at the 6P/ZnO$(10\bar{1}0)$ interface though it has been observed, for example, when depositing 6P on mica (001) or amorphous mica.[29,30]

Second, the distribution of capture zones of the islands is analysed in the aggregation regime where their density stays constant. Molecules diffusing within the capture zone are incorporated with high probability into the associated island. The borders of the capture zones coincide with the Voronoi

polygons built around the centres of the islands.[31] Normalized capture zone distributions derived from AFM images recorded after exposure times between 4 min and 14 min are depicted in Fig. 3b. The evaluation was performed with an appropriate software[32] using an optimal bin size as proposed by Scott.[33] The abscissa is rescaled according to $s = A/\langle A \rangle$ where A is the size of the capture zone and $\langle A \rangle$ the average size. Pimpinelli and Einstein showed that the capture zone distribution can be described by the generalized Wigner distribution $P_\beta(s) = a_\beta s^\beta e^{-b_\beta s^2}$ containing only one parameter β whereby a_β and b_β are constants assuring normalization and unit mean, respectively.[34] Corresponding curves calculated for $\beta = 2 - 4$ are depicted in Fig. 3b. The curve corresponding to $\beta = 2$ reproduces best the experimental data. The parameter β can be correlated to the critical nucleus size i , where $i + 1$ is the number of molecules required to form stable nuclei which eventually evolve into islands.[34] The exact relation depends, however, on the aggregation limiting process.[35] For isotropic, diffusion limited aggregation $\beta = i + 2$ holds, suggesting $i = 0$ in the present case, *i.e.*, already one molecule would form a stable nucleus which is rather unlikely. A more plausible explanation is that sub-ML growth of 6P-F_4 cannot be described within the framework of diffusion-limited aggregation.

Combining all so far obtained information, two scenarios are conceivable for the sub-ML growth of 6P-F_4 on ZnO: (1) A wetting layer grows and when it is completed, islands start to nucleate on top. The islands are composed of one layer of molecules which are considerably stronger tilted than in the bulk as the height of the islands is only 1.6 nm. (2) A wetting layer grows and eventually, when a critical amount of molecules is deposited, it starts to transform into islands. The latter, representing the energetically more stable entities, consume the metastable wetting layer in the course of the growth as schematically depicted in Fig. 3c. A similar picture has been invoked before for the growth of 6P on SiO_2 and Cu(110)2 × 1–O as well as for Rubicene on SiO_2.[21,28,36] If (2) is valid, the tilt of the molecules in the first ML is similar to that in the bulk as the actual height of the islands is close to the XRD value of the lattice spacing *d*. Furthermore, scenario (2) is also in agreement with the conclusion that in the sub-ML regime 6P-F_4 cannot be described by a diffusion-limited aggregation process. AFM and post-growth XRD measurements do not provide sufficient information to finally decide the issue. The real-time XRD-measurements presented in the next section will show, however, that indeed scenario (2) is appropriate.

3.3 *In situ* real-time X-ray investigations of the growth mode:

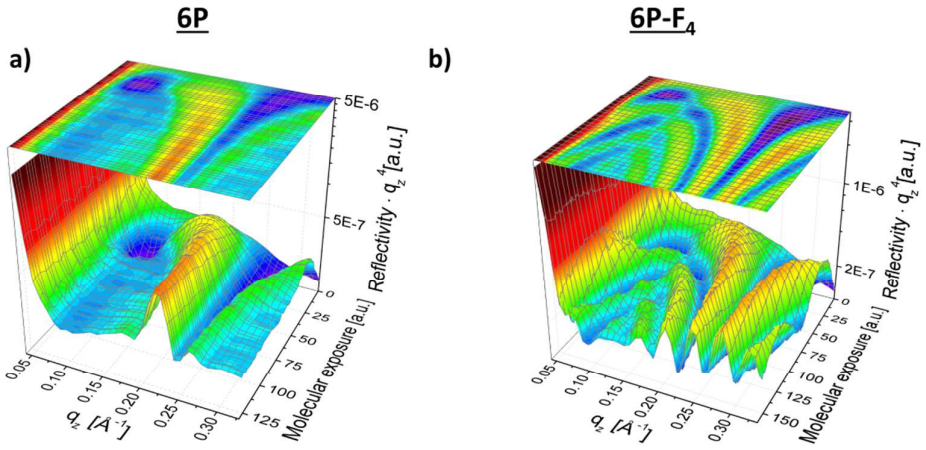

Fig. 4: Evolution of the X-ray reflectivity (multiplied by q_z^4 for better visibility) during the growth of 6P and 6P-F_4 films on ZnO$(10\bar{1}0)$. With increasing molecular exposure (*i.e.* rate · deposition time) the first order Bragg reflection gets more pronounced. While during the growth of 6P only weak Laue oscillations are observed, 6P-F_4 exhibits nearly undamped oscillations.

In addition to the AFM snapshots, which give a detailed look at the morphology during the early stages of 6P-F_4 growth, we performed real-time X-ray reflectivity measurements as shown in Fig. 4. Directly following the structural evolution during a continuous growth run allows excluding dewetting effects that might in principle affect AFM experiments which require growth interruptions. Real-time observation furthermore facilitates efficient data collection for both 6P and 6P-F_4 growth for several ML thick films. The q_z dependent reflectivity data in Fig. 4 contain rich information about the growth mode. In particular, the layer thickness and layer coverage as well as the growth speed of each ML can be extracted.

Both the 6P and the 6P-F_4 (001) Bragg reflections between 0.2 Å^{-1} and 0.3 Å^{-1} get stronger with ongoing film growth. The position of the (001) reflection shifts to higher q_z values for both molecules, which can be indicative of a surface induced change in the out-of-plane lattice spacing *d*. However, as discussed before, interference effects at small q_z values also lead to changes in Bragg peak shape and position so that we analysed also higher order reflections such as the (004) reflection shown in Fig. 5. The (004) Bragg reflection of 6P-F_4 is significantly stronger than the substrate reflectivity and clearly shifts to larger q_z values (Fig. 5). This corresponds to a decreasing lattice spacing *d* of 6P-F_4 and, thus, to stronger tilted molecules in higher layers (see table Fig 5). The *d*-value of the first ML coincides very well with the height of the islands measured by AFM in the sub-ML regime if the thickness of the wetting layer is added confirming the validity of growth scenario

(2). Grazing incidence diffraction measurements of changing in-plane lattice constants (see SI part D) confirm the surface induced structure with more upright standing 6P-F_4 molecules in the first layers. Similar findings have been reported for pentacene and diindenoperylene, dioctyl-terthiophene and sexithiophene indicating that this is a more general phenomenon.[3,4,37,38] In the case of pristine 6P, the phase coexistence and interference with the substrate reflection make it impossible to infer details about a surface induced structure since the shifting Bragg reflection is influenced by overlapping β- and γ-phase as well as substrate reflections. However, surface induced phases are also known for 6P. On ion-bombarded mica, for example, the trend is reversed with more tilted molecules at the interface. [20]

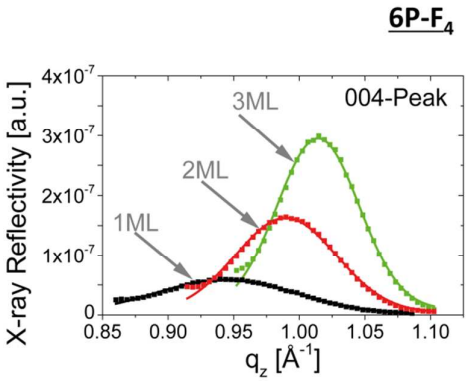

	d [nm]
1 ML	2.64 ± 0.12
2 ML	2.46 ± 0.06
3 ML	2.42 ± 0.03

Fig. 5: Left side: (004) out-of-plane Bragg reflection for 6P-F_4 films for the first three MLs. A surface induced structure that differs from the bulk is responsible for the shifting reflection. Right side: surface induced changes in the lattice spacing *d* of 6P-F_4 for the 1st, 2nd and 3rd ML as deduced from (003), (004), and (005) Bragg reflections.

For a detailed analysis of the 3D data in Fig. 4, we use two different methods. On the one hand, we take cuts at fixed q_z values of ½, ⅔, and ¾ · q_{Bragg} and analyse as a function of time the resulting growth oscillations, a technique that is frequently used in growth of inorganic[39–43] and organic materials.[44–47] On the other hand, we take cuts through the 3D data at fixed times *t* and use the Parratt formalism[48] to determine the electron density distribution of the films at each point in time.

In Fig. 6 the evolution of the intensity of the specular reflected beam during the growth of 6P (a) and 6P-F_4 (b) is shown for three different q_z positions: ½q_{Bragg} (Anti-Bragg point), ⅔q_{Bragg} and ¾q_{Bragg} as a function of *molecular exposure = (exposure time) · (molecular flux)*. Growth oscillations originate from alternating constructive and destructive interferences between the scattered beams from the individual molecular MLs. At the so called anti-Bragg position q_z = ½q_{Bragg} successive layers interfere destructively, *i.e.*, the first molecular layer reduces the ZnO reflectivity, the second layer increases the reflectivity, the third layer reduces the reflectivity again and so on.[39] Oscillations of the X-ray reflectivity are also observed at other q_z points, however, the oscillation period changes from being 2

ML at the ½q_{Bragg} anti-Bragg point, to 3 ML at ⅔q_{Bragg} and 4 ML at ¾q_{Bragg}.[49,50] As shown in Fig. 6 for 6P, the ½q_{Bragg} oscillations are damped out quickly as the surface roughens during island growth, while for 6P-F_4 the oscillations continue during the smooth layer-by-layer growth.

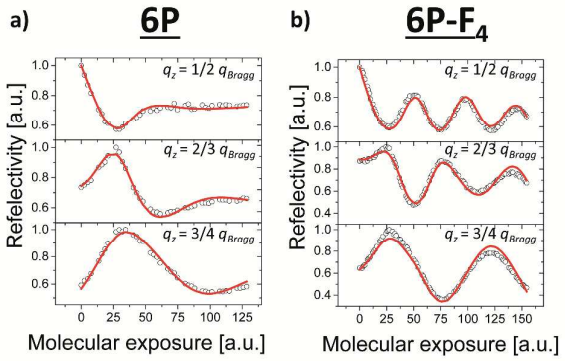

Fig. 6: 6P (a) and 6P-F_4 (b) growth oscillations at three positions of q_z as a function of molecular exposure. The red lines show the best fits using the Trofimov model of the experimental values.

For a quantitative analysis, we fit the growth oscillations at three different q_z points simultaneously to extract the layer coverages for each ML of upright-standing molecules as a function of time. To extract this information, we calculate the X-ray reflectivity using a lattice sum where the substrate scattering as well as the scattering from every layer is added. We take into account the coverage of each layer at a given point in time and, importantly, also the changes in the 6P-F_4 layer thicknesses for the first MLs (for details see SI part E). However, for simplicity, we do not include the wetting layer of lying down molecules which exists for the very beginning of growth on the ZnO. The time dependent layer coverages that enter this lattice sum are simulated using an atomistic, rate-equation model of growth developed by Trofimov *et al.*[51] as previously applied in a simplified form in references[52–54] and detailed in the SI part E. In Fig. 6, the red lines represent the best fits based on that model to the experimental values shown as dots (see SI part E for best fit parameters). The resulting layer coverages are shown in Fig. 7a and b.

Our second, independent analysis of the 3D data in Fig. 5 uses the Parratt formalism[48] and results in layer coverage curves as shown in Fig. 7a and b. In the Parratt approach, the real-space structure at a fixed time during growth is divided into stratified layers, corresponding to the substrate and each molecular ML. Again, for simplicity we consider only upright standing molecules and do not introduce an additional stratified layer for the wetting layer, which in any case only influences the very beginning of the growth and mostly changes the reflectivity at q_z – values larger than the q_z range in the real-time experiments. Therefore the sensitivity of the fit is not large enough to distinguish between the presence or absence of a wetting layer. For this layered structure, the X-ray reflectivity

is then calculated using the optical transfer matrix method with the thickness and the electron density of each layer as fit parameters (see SI part F). This approach also confirms that the thickness of the first 6P-F_4 layers is changing due to a surface induced structure. Furthermore, the electron densities of the 6P-F_4 respectively 6P layers follow s-shaped curves, which, when normalized to the value of the electron density of a filled layer, agree with the coverage curves of the model of Trofimov *et al.* within better than 10 % for 6P-F_4 and better than 20 % for 6P. In addition the evaluation of the AFM pictures shown in Fig. 3a allows us to determine the coverage dependence for the 6P-F_4 directly, which is then compared to the X-ray data. This is depicted on the right side of Fig. 7b where the real-time X-ray data evaluated by the model of Trofimov *et al.* for the first MLs is compared with the AFM data from snapshots during growth. Very good agreement between these data sets is found. Considering the different methods for determining the coverage, the AFM data points are nearly perfectly coinciding with the lines given by the model of Trofimov *et al.*.

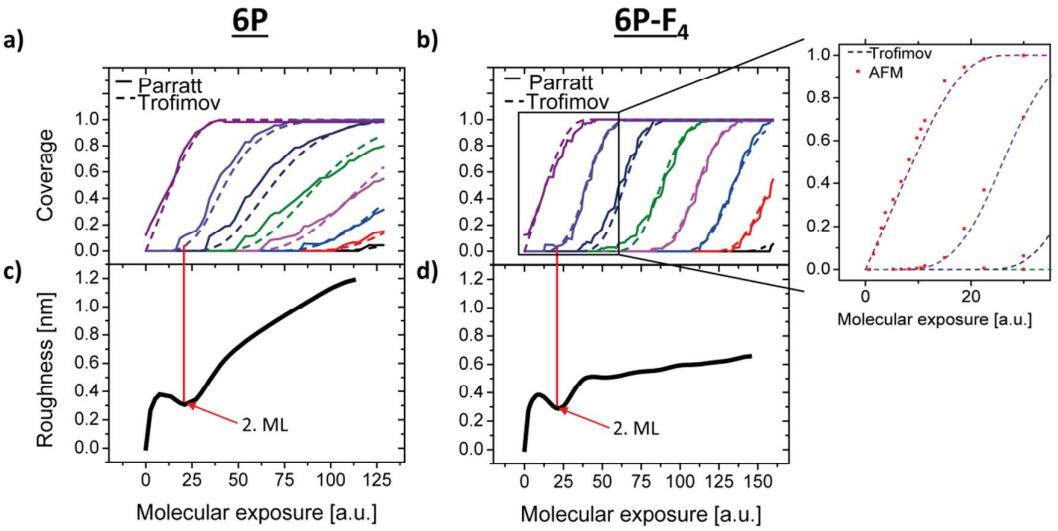

Fig 7: Comparison of the calculated layer coverages by using the Trofimov model and fits of the *in situ* XRR curves based on the Parratt formalism for 6P (a) and 6P-F_4 (b). Enlargement in (b) demonstrates excellent agreement in layer coverage curves between AFM data and the Trofimov model. c) and d) calculated RMS roughness during the film growth.

The layer coverage curves in Fig. 7a and b give a detailed picture of the different growth modes of 6P and the 6P-F_4. While for both molecules the first layer is more than 75 % complete before the second layer reaches a coverage of 5%, the growth mode starts to differ significantly from the second ML onwards. For 6P a 3D island growth mode sets in, as the third and even fourth layer start to grow simultaneously with the second layer as evidenced by the shallow coverage curves. In the case of the 6P-F_4 growth the coverage curves show a steep slope up to at least the 7th ML, *i.e.*, growth proceeds in a layer-by-layer mode.

Knowing the ML thickness and the ML coverage, the root-mean-square (RMS) roughness can be calculated. The resulting curves are shown in Fig. 7c and d. The roughness evolution of 6P has a minimum, when the smooth surface of the first ML is completed, but then a significant increase of the roughness occurs with the beginning of the second ML growth as shown in Fig. 7c. In contrast the roughness curve for 6P-F_4 shows slight minima every time the islands within a ML have coalesced resulting in a smooth continuous film. The fact that this minimum is not zero implies that the layer-by-layer growth is not fully ideal, which can also be seen in the coverage curves. Nevertheless, a comparison of 6P and 6P-F_4 roughness curves in Fig. 7c and d clearly shows that the 3D growth of 6P results in a surface roughness which, for comparable film thickness, is twice as high as in the case of the layer-by-layer growth of 6P-F_4.

5 Discussion

All performed experiments conclusively show that terminal fluorination of 6P causes a transition from a 3D growth for the parent 6P to an almost 2D growth mode for 6P-F_4 on ZnO$(10\overline{1}0)$. In the following we discuss factors which may contribute to this pronounced change.

The fluorination of 6P in the four “corner” positions changes intermolecular electrostatic interactions through the introduction of two local dipole moments at both molecular termini. The crystal cohesive energy will thus be different for the two molecules. Furthermore, a flat-lying 6P-F_4 molecule diffusing on the surface of an island exposing fluorine atoms at its boundary will experience a substantially altered binding energy as compared to 6P where the islands are presenting hydrogen at their periphery. As a consequence, the activation energy for molecules diffusing on islands as well as the Ehrlich-Schwoebel barrier, both critical parameters in a kinetically controlled growth process, will differ. Indeed an increase of the Ehrlich-Schwoebel barrier with increasing crystal cohesive and surface binding energies has been predicted.[55] Our result of 6P-F_4 layer-by-layer growth therefore suggests that both cohesive as well as binding energies are reduced by terminal fluorination. Theoretical input is required to verify the sign and to assess the magnitude of the change in the energy terms.

The physical size of 6P and 6P-F_4 molecules is nearly identical. However, changes in the intermolecular electrostatic interactions as well as possibly weak C-H…F-H bonding cause subtle changes in the structure of the bulk phase of the films where the molecular tilt angle of 6P-F_4 is larger than for 6P. This tilt angle has also been correlated to the magnitude of the Ehrlich-Schwoebel barrier.[20,56] For rod-like molecules, a larger molecular tilt has been related to a smaller step edge barrier since less energy is required to bend the molecule around an island boundary during its

downward movement. Thus, the change in the geometric arrangement of the molecules in the bulk phase of the films induced by terminal fluorination also contributes to enhanced downward mass transport facilitating layer-by-layer growth.[20] In the thin-film-phase close to the interface, a surface induced structure was resolved for 6P-F_4. In the first three 6P-F_4 MLs, the molecular tilt angle changes gradually from more upright standing to slightly tilted. Therefore, one would expect the more upright standing surface induced phase to increase the Ehrlich-Schwoebel barrier and hinder layer-by-layer growth at the initial growth stage. Our results suggest that this effect is counterbalanced by better molecular diffusivity due to a lower surface energy. Its minimisation is the driving force behind such a surface induced structure so that for more upright standing molecules the surface energy is apparently lower than for tilted molecules found in the bulk phase of the film. A lower surface energy on top of the first monolayers leads to enhanced diffusivity of admolecules and therefore contributes to better layer-by-layer growth. Similar to the present case, a surface induced phase with more upright standing molecules has been correlated with layer-by-layer growth in the similar molecular system diindenoperylene.[54,57] While the ML growth of 6P-F_4 proceeds via a wetting layer, for 6P no indication for the presence of a wetting layer was found. Nucleation of the second layer starts for both molecules when the ZnO surface is almost completely covered by islands and a roughening of the 6P film sets in only in the course of the growth of the second layer. Therefore we conclude that the wetting layer has only a minor effect on the growth mode. Another difference is the coexistence of the β- and γ-phase in 6P films while 6P-F_4 grows in a single phase. Grain boundaries occurring between different phases can act as nucleation sites for succeeding layers and thus cause roughening.

Finally we discuss the impact of the ZnO surface preparation on the structure and morphology of the organic layer. While the growth mode of the molecules, 3D vs. 2D, is not affected by the surface treatment, we find changes in the epitaxial relation with the substrate in case of 6P. On epitaxial ZnO surfaces used in AFM experiments, 6P molecules show a preferred in plane orientation, namely the projection of the long molecular axis (mounds) or the long molecular axis (needles) are orientated parallel to ZnO$[010]$. Such orientation is induced by the dipolar surface field present at the ZnO$(10\bar{1}0)$ surface.[19] On the sputter/annealed ZnO surface, on the contrary, we find neither a preferred in-plane orientation nor formation of needle-shaped crystallites with flat lying molecules. Apparently, an intrinsic, non-passivated ZnO surface is essential to align the molecules in the surface field.

6 Conclusion

Combined *in situ* AFM and *in situ* real-time X-ray studies demonstrate that a subtle chemical modification of 6P by terminal fluorination substantially alters the growth mode and the resulting thin film structure. Most prominently, terminal fluorination enhances downward mass transport through a combination of increased surface diffusivity and a lower Ehrlich-Schwoebel barrier, leading to a smooth almost layer-by-layer thin film growth. Characteristic features of the thin films are summarised in Fig. 8.

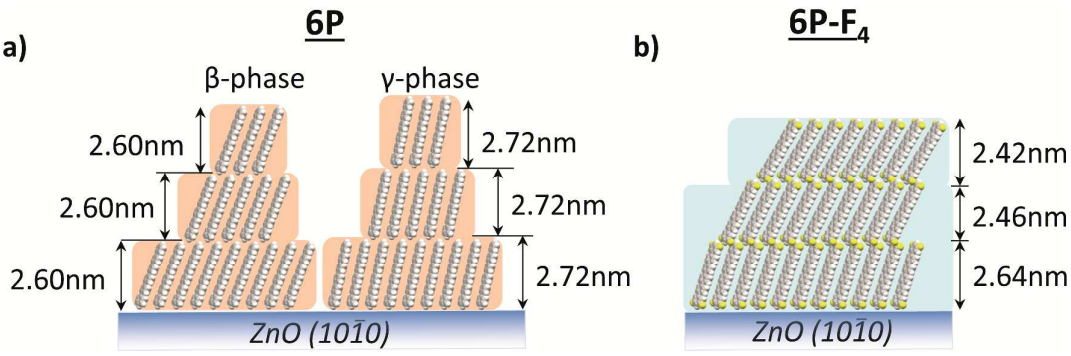

Fig. 8: Schematic drawing of the rough 6P growth with two different polymorphs (a) and smooth 6P-F_4 growth with surface induced structure.

For both molecules we find a high degree of crystallinity with molecules essentially standing upright when deposited at room temperature on ZnO($10\bar{1}0$). While in 6P thin films, β and γ phases coexist, 6P-F_4 grows in a single phase, although the molecular tilt angle gradually increases within the first three layers. In case of 6P, our experiments do not provide conclusive evidence for the presence or absence of such a surface induced structure. However, the most striking difference is the change from 3D for 6P to an almost 2D morphology for its fluorinated derivative. Our results demonstrate thus that selective fluorination can decisively alter growth processes and film roughness and therefore presents a viable strategy to produce crystalline organic layers with thin film morphologies tailored for use in opto-electronic devices.

Acknowledgements:

We are grateful to R. Felici at ESRF for providing assistance in using beamline ID03, and to M. Gensler for help with AFM experiments. This work was enabled by financial support through the collaborative research center SFB951.

7 References:

1. S. Blumstengel, S. Sadofev, and F. Henneberger, *New J. Phys.*, 2008, **10**, 065010.

2. G. Hlawacek and C. Teichert, *J. Phys. Condens. Matter*, 2013, **25**, 143202.

3. S. Kowarik, A. Gerlach, S. Sellner, L. Cavalcanti, O. Konovalov, and F. Schreiber, *Appl. Phys. A*, 2009, **95**, 233–239.

4. S. Schiefer, M. Huth, A. Dobrinevski, and B. Nickel, *J. Am. Chem. Soc.*, 2007, **129**, 10316–7.

5. I. Salzmann, D. Nabok, M. Oehzelt, S. Duhm, A. Moser, G. Heimel, P. Puschnig, C. Ambrosch-Draxl, J. P. Rabe, and N. Koch, *Cryst. Growth Des.*, 2011, **11**, 600–606.

6. M. Schiek, F. Balzer, K. Al-Shamery, A. Lützen, and H.-G. Rubahn, *Soft Matter*, 2008, **4**, 277.

7. D. Kühne, F. Klappenberger, R. Decker, U. Schlickum, H. Brune, S. Klyatskaya, M. Ruben, and J. V. Barth, *J. Phys. Chem. C*, 2009, **113**, 17851–17859.

8. S. Tasch, C. Brandstatter, F. Meghdadi, G. Leising, G. Froyer, and L. Athouel, *Adv. Mater.*, 1997, **9**, 33–36.

9. C. Simbrunner, G. Hernandez-Sosa, E. Baumgartner, G. Hesser, J. Roither, W. Heiss, and H. Sitter, *Appl. Phys. Lett.*, 2009, **94**, 073505.

10. T. Mikami and H. Yanagi, *Appl. Phys. Lett.*, 1998, **73**, 563.

11. F. Quochi, F. Cordella, A. Mura, G. Bongiovanni, F. Balzer, and H.-G. Rubahn, *Appl. Phys. Lett.*, 2006, **88**, 041106.

12. R. Resel, *Thin Solid Films*, 2003, **433**, 1–11.

13. R. Resel, *J. Phys. Condens. Matter*, 2008, **20**, 184009.

14. C. Simbrunner, *Semicond. Sci. Technol.*, 2013, **28**, 053001.

15. S. Blumstengel, H. Glowatzki, S. Sadofev, N. Koch, S. Kowarik, J. P. Rabe, and F. Henneberger, *Phys. Chem. Chem. Phys.*, 2010, **12**, 11642.

16. J. Novák, M. Oehzelt, S. Berkebile, M. Koini, T. Ules, G. Koller, T. Haber, R. Resel, and M. G. Ramsey, *Phys. Chem. Chem. Phys.*, 2011, **13**, 14675–84.

17. K. N. Baker, A. V. Fratini, T. Resch, H. C. Knachel, W. W. Adams, E. P. Socci, and B. L. Farmer, *Polymer (Guildf).*, 1993, **34**, 1571–1587.

18. R. Resel, N. Koch, F. Meghdadi, G. Leising, L. Athouel, G. Froyer, and F. Hofer, *Cryst. Res. Technol.*, 2001, **36**, 47–54.

19. F. Della Sala, S. Blumstengel, and F. Henneberger, *Phys. Rev. Lett.*, 2011, **107**, 146401.

20. G. Hlawacek, P. Puschnig, P. Frank, A. Winkler, C. Ambrosch-Draxl, and C. Teichert, *Science (80-.).*, 2008, **321**, 108–111.

21. P. Frank, G. Hlawacek, O. Lengyel, A. Satka, C. Teichert, R. Resel, and A. Winkler, *Surf. Sci.*, 2007, **601**, 2152–2160.

22. T. Potocar, S. Lorbek, D. Nabok, Q. Shen, L. Tumbek, G. Hlawacek, P. Puschnig, C. Ambrosch-Draxl, C. Teichert, and A. Winkler, *Phys. Rev. B*, 2011, **83**, 075423.

23. J. Götzen and G. Witte, *Appl. Surf. Sci.*, 2012, **258**, 10144–10147.

24. S. Sadofev, S. Blumstengel, J. Cui, J. Puls, S. Rogaschewski, P. Schäfer, and F. Henneberger, *Appl. Phys. Lett.*, 2006, **89**, 201907.

25. L. O. Péres, F. Guillet, and G. Froyer, *Org. Biomol. Chem.*, 2004, **2**, 452–454.

26. D. Nečas and P. Klapetek, *Cent. Eur. J. Phys.*, 2011, **10**, 181–188.

27. D. Nabok, P. Puschnig, and C. Ambrosch-Draxl, *Phys. Rev. B*, 2008, **77**, 245316.

28. B. Scherwitzl, W. Lukesch, A. Hirzer, J. Albering, G. Leising, R. Resel, and A. Winkler, *J. Phys. Chem. C. Nanomater. Interfaces*, 2013, **117**, 4115–4123.

29. C. Teichert, G. Hlawacek, A. Y. Andreev, H. Sitter, P. Frank, A. Winkler, and N. S. Sariciftci, *Appl. Phys. A*, 2005, **82**, 665–669.

30. L. Tumbek, C. Gleichweit, K. Zojer, and A. Winkler, *Phys. Rev. B*, 2012, **86**, 085402.

31. P. Mulheran and J. Blackman, *Phys. Rev. B*, 1996, **53**, 10261–10267.

32. U. Rasband, W.S., ImageJ 1.46, U. S. National Institutes of Health, Bethesda, Maryland, .

33. D. W. Scott, *Biometrika*, 1979, **66**, 605–610.

34. A. Pimpinelli and T. Einstein, *Phys. Rev. Lett.*, 2007, **99**, 226102.

35. A. Pimpinelli, L. Tumbek, and A. Winkler, *J. Phys. Chem. Lett.*, 2014, **5**, 995–998.

36. A. J. Fleming, F. P. Netzer, and M. G. Ramsey, *J. Phys. Condens. Matter*, 2009, **21**, 445003.

37. O. Werzer, N. Boucher, J. P. de Silva, G. Gbabode, Y. H. Geerts, O. Konovalov, A. Moser, J. Novak, R. Resel, and M. Sferrazza, *Langmuir*, 2012, **28**, 8530–6.

38. J.-F. Moulin, F. Dinelli, M. Massi, C. Albonetti, R. Kshirsagar, and F. Biscarini, *Nucl. Instruments Methods Phys. Res. Sect. B Beam Interact. with Mater. Atoms*, 2006, **246**, 122–126.

39. H. van der Vegt, H. van Pinxteren, M. Lohmeier, E. Vlieg, and J. Thornton, *Phys. Rev. Lett.*, 1992, **68**, 3335–3338.

40. E. Weschke, C. Schüßler-Langeheine, R. Meier, G. Kaindl, C. Sutter, D. Abernathy, and G. Grübel, *Phys. Rev. Lett.*, 1997, **79**, 3954–3957.

41. C. Nicklin, M. Everard, C. Norris, and S. Bennett, *Phys. Rev. B*, 2004, **70**, 235413.

42. A. Fleet, D. Dale, A. R. Woll, Y. Suzuki, and J. D. Brock, *Phys. Rev. Lett.*, 2006, **96**, 055508.

43. M. Hanke, V. M. Kaganer, O. Bierwagen, M. Niehle, and A. Trampert, *Nanoscale Res. Lett.*, 2012, **7**, 203.

44. B. Krause, F. Schreiber, H. Dosch, A. Pimpinelli, and O. H. Seeck, *Europhys. Lett.*, 2004, **65**, 372–378.

45. A. Mayer, R. Ruiz, H. Zhou, R. Headrick, A. Kazimirov, and G. Malliaras, *Phys. Rev. B*, 2006, **73**, 205307.

46. A. Amassian, T. V Desai, S. Kowarik, S. Hong, A. R. Woll, G. G. Malliaras, F. Schreiber, and J. R. Engstrom, *J. Chem. Phys.*, 2009, **130**, 124701.

47. S. Y. An, K. Ahn, D. Y. Kim, H.-H. Lee, J. H. Cho, and D. R. Lee, *J. Chem. Phys.*, 2014, **140**, 154702.

48. L. Parratt, *Phys. Rev.*, 1954, **95**, 359–369.

49. S. Kowarik, A. Gerlach, M. W. A. Skoda, S. Sellner, and F. Schreiber, *Eur. Phys. J. Spec. Top.*, 2009, **167**, 11–18.

50. S. Kowarik, A. Gerlach, W. Leitenberger, J. Hu, G. Witte, C. Wöll, U. Pietsch, and F. Schreiber, *Thin Solid Films*, 2007, **515**, 5606–5610.

51. V. I. Trofimov and V. G. Mokerov, *Thin Solid Films*, 2003, **428**, 66–71.

52. A. R. Woll, T. V. Desai, and J. R. Engstrom, *Phys. Rev. B*, 2011, **84**, 075479.

53. C. Weber, C. Frank, S. Bommel, T. Rukat, W. Leitenberger, P. Schäfer, F. Schreiber, and S. Kowarik, *J. Chem. Phys.*, 2012, **136**, 204709.

54. C. Frank, J. Novák, R. Banerjee, A. Gerlach, F. Schreiber, A. Vorobiev, and S. Kowarik, *Phys. Rev. B*, 2014, **90**, 045410.

55. J. E. Goose, E. L. First, and P. Clancy, *Phys. Rev. B*, 2010, **81**, 205310.

56. X. Zhang, E. Barrena, D. Goswami, D. de Oteyza, C. Weis, and H. Dosch, *Phys. Rev. Lett.*, 2009, **103**, 136101.

57. S. Kowarik, A. Gerlach, S. Sellner, F. Schreiber, L. Cavalcanti, and O. Konovalov, *Phys. Rev. Lett.*, 2006, **96**, 125504.